PHOTONICS Research

Weak-value amplification for the optical signature of topological phase transitions

WEIJIE WU,[1,2] SHIZHEN CHEN,[1] WENHAO XU,[1] ZHENXING LIU,[3] RUNNAN LOU,[2] LIHUA SHEN,[2] HAILU LUO,[1,4] 🔵
SHUANGCHUN WEN,[1] AND XIAOBO YIN[2,3,5]

[1]*Laboratory for Spin Photonics, School of Physics and Electronics, Hunan University, Changsha 410082, China*
[2]*Department of Mechanical Engineering, University of Colorado, Boulder, Colorado 80309, USA*
[3]*Materials Science and Engineering Program, University of Colorado, Boulder, Colorado 80309, USA*
[4]*e-mail: hailuluo@hnu.edu.cn*
[5]*e-mail: xiaobo.yin@colorado.edu*

We show that weak measurements can be used to measure the tiny signature of topological phase transitions. The signature is an in-plane photonic spin Hall effect, which can be described as a consequence of a Berry phase. It is also parallel to the propagation direction of a light beam. The imaginary part of the weak value can be used to analyze ultrasmall longitudinal phase shifts in different topological phases. These optical signatures are related to the Chern number and bandgaps; we also use a preselection and postselection technique on the spin state to enhance the original signature. The weak amplification technique offers a potential way to determine the spin and valley properties of charge carriers, Chern numbers, and topological phases by direct optical measurement.   © 2020 Chinese Laser Press

https://doi.org/10.1364/PRJ.401531

1. INTRODUCTION

Topological physics has recently attracted great attention due to its fundamental scientific importance and potential application in novel optoelectronic devices [1–6]. Silicene, which consists of silicon atoms [7,8], with a monolayer honeycomb system is a prime candidate. Unlike graphene, silicene is nonplanar and possesses intrinsic spin-orbit coupling that provides a mass to Dirac electrons; it also favors an experimentally accessible Kane–Mele type quantum spin Hall effect [9,10]. It is remarkable that the mass can be controlled by an external electric field and/or circularly polarized light [11,12], which leads to topological phase transitions in silicene. The Chern number, as a topological invariant, is associated with a band, and it is the integral of the Berry curvature over the entire Brillouin zone [13]. Further, Berry curvature is a function of wave vectors. Measurement of the Chern number plays an important role in the determination of different topological phases. However, one of the most challenging goals is how to measure the Chern number and different topological states in a direct and facile way.

Here, considering that Hall conductivity can be directly reflected by an optical signature, we investigate the signature amplified by weak measurement [14]. An in-plane photonic spin Hall effect (SHE) and longitudinal phase shifts can be a new spin-sensitive topological probe [15]. A fundamental origin of the photonic SHE is related to the spin-orbit interaction. The ubiquitous effect is often used as a metrological tool [16–20] because of its high sensitivity to the physical properties of materials. This provides a novel measuring method for the metrology community [21–23].

This paper presents an optical signature for probing low-energy Dirac-like physics in systems that can realize topological phase transitions. It is valuable since an optical signature will make this important physics more accessible to the metrology community. The in-plane photonic SHE serves as an optical probe by virtue of the spatial splitting and angular deviations of its reflected beam. We can observe different Hall transitions while silicene samples were exposed to externally applied circularly polarized lasers and/or static electric fields. While Ref. [24] considered transverse splitting, its system did not exhibit weak measurement. This weak value amplification technique can be applied to enhance the original tiny signature, achieving a sensitivity to ∼0.5 mm (∼1 milliradian). Further, Brunner and Simon present a purely imaginary weak value that can detect phase shifts, which has potential to outperform standard interferometry by three orders of magnitude [25]. We apply this progressive method to probe topological phase transitions on 2D atomic crystals. Thus, the optical signature that is amplified by weak measurement provides a feasible scheme for observing the Chern number and topological phase transitions.

2. TOPOLOGICAL PHASE TRANSITIONS AND OPTICAL SIGNATURE

We consider optical reflection from an air–silicene interface to measure signals of topological phase transition. Due to the refractive index gradient, the momentum can be transferred between the spin and extrinsic orbital angular momentum of light along its propagation trajectory, resulting in beam splitting with polarizations [26]. The beam splitting in the photonic SHE, impinging on an anisotropic medium, occurs, respectively, in the transverse and in-plane directions [27]. The transverse splitting, implied by angular momentum conservation [24,28,29], is ubiquitous, while the in-plane splitting only occurs on an anisotropic medium [30]. The cross-polarization can cause in-plane splitting [31]. Further, the Hall conductivity gives a non-negligible contribution to the cross-polarization [32,33]. The in-plane photonic SHE is distinguished from the Goos–Hänchen effect [34]. Because the former is spin-dependent, and it takes place as a result of an effective spin-orbit interaction, the latter is polarization-dependent, which is described in terms of evanescent wave penetration. Remarkably, spin-sensitive topological phase transition requires a spin-sensitive measurement. Here, we propose to take the in-plane splitting as an optical probe of weak measurement to detect topological phase transitions. Thus, a phase estimation technique is introduced to complete the entire detection system.

Figure 1 illustrates that a Gaussian beam of frequency ω_0 impinges at an angle θ_i on a silicene placed on top of a SiC substrate of dielectric constant ϵ. The system is subject to a static electric field and circularly polarized light. The corresponding electromagnetic potential is given by $A(t) = (A_0 \sin \omega t, A_0 \cos \omega t)$, where $\omega \gg \omega_0$ is the frequency of circularly polarized light with $\omega < 0\,(\omega > 0)$ specifying left (right) circular polarization and A_0 is the amplitude.

The low-energy effective Hamiltonian is derived in the momentum space [35–37]. We have

$$H_\eta = \hbar \nu_F (\eta k_x \tau_x + k_y \tau_y) + \lambda_{SO} \sigma_z \eta \tau_z - e\ell E_z \tau_z - \Lambda \eta \tau_z. \quad (1)$$
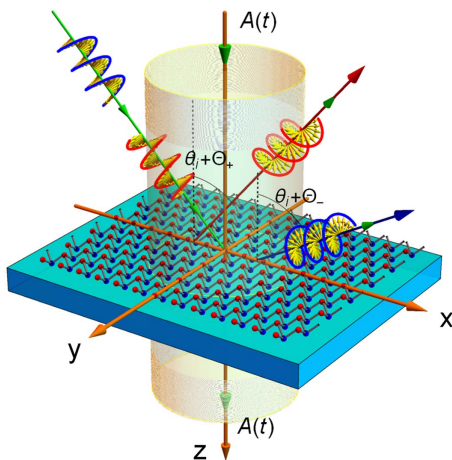
Fig. 1. Schematic representation of the wave reflection from an air–silicene interface. The system is subject to a static electric field E_z, which is opposite the z axis, and to circularly polarized lasers. The lattice constant is $a = 3.86$ Å, staggering length value is $\ell = 0.23$ Å, and the effective spin-orbit coupling is $\lambda_{SO} = 3.9$ meV.

Here, $\sigma = (\sigma_x, \sigma_y, \sigma_z)$ and $\tau = (\tau_x, \tau_y, \tau_z)$ are the Pauli matrices of the spin and the sublattice pseudospin, respectively; $\eta = \pm 1$ is the valley index, ν_F is the Fermi velocity, λ_{SO} is the effective spin-orbit (SO) coupling, ℓ is the buckled height, E_z is the perpendicular electric field, and Λ is the coupling constant between the monolayer and the circularly polarized light. By diagonalizing the Hamiltonian in Eq. (1), the bandgap is given by $2|m_s^\eta|$ with the Dirac mass:

$$m_s^\eta = \eta s \lambda_{SO} - e\ell E_z - \eta \Lambda. \quad (2)$$

Here, $\Lambda = (eaA_0\nu_F)^2 \hbar / \omega_0$, and a is the lattice constant. From Eq. (2), the Dirac mass can be controlled by applying electric field E_z and coherent laser beam.

In addition, the nontrivial topological feature can also be characterized by the Chern number. In the momentum space, the vector Berry connection is defined as $\mathcal{A}_i(\vec{k}) = -i\langle \psi(\vec{k})| \frac{\partial}{\partial k_i} |\psi(\vec{k})\rangle$, where $\psi(\vec{k})$ is the eigenvector of the Hamiltonian. The Berry curvature is $\mathcal{F}(\vec{k}) = \partial \mathcal{A}_y(\vec{k}) / (\partial k_x) - \partial \mathcal{A}_x(\vec{k}) / (\partial k_y)$. Since the different states correspond to different beam shifts, the Berry curvature can also be distinguished by photonic SHE [38,39]. It is calculated in Fig. 2(h).

The Chern number is the integral of the Berry curvature $\mathcal{F}(\vec{k})$ over the first Brillouin zone. It is also associated to a band
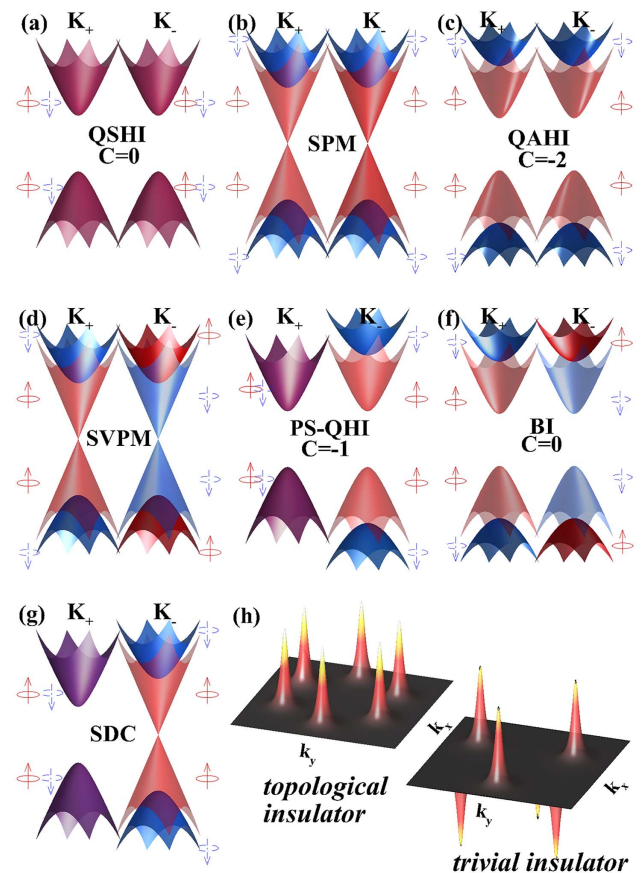
Fig. 2. Electronic band structure of silicene for K and K' point in the states of (a) QSHI, (b) SPM, (c) QAHI, (d) SVPM, (e) PS-QHI, (f) BI, and (g) SDC. The red arrow (blue arrow) is for up-spin (down-spin) electrons. (h) Berry curvature $\mathcal{F}(\vec{k})$ can distinguish the topological insulator and trivial insulator.

provided the gap is open. It is determined by the Dirac mass and the valley index, that is, $\mathcal{C}_s^{\eta} = \eta \mathrm{sgn}(m_s^{\eta})/2$. Then, the Chern number is obtained by $\mathcal{C} = \sum_{\eta=\pm}(\mathcal{C}_+^{\eta} + \mathcal{C}_-^{\eta})$. The Chern number $\mathcal{C}$ is shown in Fig. 2. In Figs. 2(a)–2(c), we show that, if we increase Λ (the initial value $\Lambda = 0$) while keeping $E_z = 0$, these gaps close at $\Lambda = \lambda_{\mathrm{SO}}$, where silicene is a semi-metal. The spin-polarized metal (SPM) appears at this point. It has the identical spin configuration at K and K' points. Further increasing Λ, the gap is reopened. And the Chern number changes, indicating that a system is continuously deformed into a new state from the previous state, namely, a topological phase transition occurs. Similar transitions can appear by changing E_z in Figs. 2(a), 2(d), and 2(f). The system undergoes topological phase transitions from a quantum spin Hall insulator (QSHI) into a quantum anomalous Hall insulator (QAHI) or a band insulator (BI). These gaps will also close when $|E_z|$ reaches a critical value. The spin-valley-polarized metal (SVPM) emerges at this point between the QSHI and BI. In Fig. 2(g), a single Dirac cone (SDC) state emerges along the phase boundaries, where the gap is open at the K point but closed at the K' point. Further increasing Λ and E_z from QSHI, the silicene reaches the photoinduced spin-polarized quantum Hall insulator (PS-QHI) phase in Fig. 2(e).

The expressions for the longitudinal and transverse conductivities with zero temperature can be obtained by Kubo's formula [24,40–42]; we have

$$
\frac{\tilde{\sigma}_{xx}^{\eta s}}{\sigma_0/2\pi} = \frac{4\mu^2 - |m_s^{\eta}|^2}{2\hbar\mu\Omega}\Theta(2\mu - |m_s^{\eta}|) + \left(1 - \frac{|m_s^{\eta}|^2}{\hbar^2\Omega^2}\right)
$$

$$
\times \arctan\left(\frac{\hbar\Omega}{M}\right) + \frac{|m_s^{\eta}|^2}{\hbar\Omega M}, \frac{\tilde{\sigma}_{xy}^{\eta s}}{\sigma_0/2\pi}
$$

$$
= \frac{2\eta m_s^{\eta}}{\hbar\Omega}\arctan\left(\frac{\hbar\Omega}{M}\right). \qquad (3)
$$

Here, $\Omega = -i\omega + \Gamma$, where Γ is the scattering rate. $\sigma_0 = e^2/4\hbar$, $\tilde{\sigma}_{xx}^{\eta s} = \tilde{\sigma}_{yy}^{\eta s}$, $\tilde{\sigma}_{xy}^{\eta s} = -\tilde{\sigma}_{yx}^{\eta s}$, and $M = \max(|m_s^{\eta}|, 2|\mu|)$.

The reflected amplitudes can be obtained by solving Maxwell's equations and imposing the appropriate boundary conditions, $\mathbf{E}_i + \mathbf{E}_r = \mathbf{E}_t$ and $\mathbf{H}_i + \mathbf{H}_r - \mathbf{H}_t = \mathbf{J}$. We decompose the incoming field into its h and v components. Sequentially, the four Fresnel's reflection coefficients, r_{ij} for incoming i-polarized and outgoing j-polarized waves, are obtained [43,44]:

$$
r_{hh} = \frac{\alpha_-\beta_+ + \sigma_{hv}\sigma_{vh}}{\alpha_+\beta_+ + \sigma_{hv}\sigma_{vh}}, \qquad r_{vv} = \frac{\alpha_+\beta_- - \sigma_{hv}\sigma_{vh}}{\alpha_+\beta_+ + \sigma_{hv}\sigma_{vh}},
$$

$$
r_{hv} = -\frac{2}{Z_i}\frac{\sigma_{hv}}{\alpha_+\beta_+ + \sigma_{hv}\sigma_{vh}}, \qquad r_{vh} = \frac{2}{Z_i}\frac{\sigma_{vh}}{\alpha_+\beta_+ + \sigma_{hv}\sigma_{vh}}. \qquad (4)
$$

Here, $Z_t = 1/\sqrt{\epsilon_t}$, $\alpha_+ = \sigma_{hh}k_{iz}/k_i + k_{iz}k_t/(Z_t k_i k_{tz}) + 1/Z_i$, $\alpha_- = \sigma_{hh}k_{iz}/k_i + k_{iz}k_t/(Z_t k_i k_{tz}) - 1/Z_i$, $\beta_+ = -\sigma_{vv}k_i/k_{iz} - k_i k_{tz}/(Z_t k_{iz}k_t) - 1/Z_i$, $\beta_- = \sigma_{vv}k_i/k_{iz} + k_i k_{tz}/(Z_t k_{iz}k_t) - 1/Z_i$, $Z_i = 1/\sqrt{\epsilon_i}$, and k_i is the wavenumber.

For horizontal polarization state $|H\rangle$ and vertical polarization state $|V\rangle$, the reflected polarization states can be written as $[|H(k_r)\rangle|V(k_r)\rangle]^T = M_R[|H(k_i)\rangle|V(k_i)\rangle]^T$. Here, M_R can be expressed as

$$
\begin{pmatrix} r_{hh} & r_{hv} \\ r_{vh} & r_{vv} \end{pmatrix}. \qquad (5)
$$

In the above equation, the boundary condition is $k_{rx} = -k_{ix}$ and $k_{ry} = k_{iy}$. By making use of Taylor series expansion based on the arbitrary angular spectrum component, all Fresnel's reflection coefficients r_{ij} can be expanded as a polynomial of k_{ix}. Then, we have

$$
|H(k_i)\rangle \rightarrow \left(r_{hh} - \frac{k_{rx}}{k_0}\frac{\partial r_{hh}}{\partial\theta_i}\right)|H(k_r)\rangle
$$

$$
+ \left(r_{vh} - \frac{k_{rx}}{k_0}\frac{\partial r_{vh}}{\partial\theta_i}\right)|V(k_r)\rangle, \qquad (6)
$$

$$
|V(k_i)\rangle \rightarrow \left(r_{hv} - \frac{k_{rx}}{k_0}\frac{\partial r_{hv}}{\partial\theta_i}\right)|H(k_r)\rangle
$$

$$
+ \left(r_{vv} - \frac{k_{rx}}{k_0}\frac{\partial r_{vv}}{\partial\theta_i}\right)|V(k_r)\rangle. \qquad (7)
$$

The polarization states of $|H\rangle$ and $|V\rangle$ are decomposed into two spin components $|H\rangle = (|+\rangle + |-\rangle)/\sqrt{2}$ and $|V\rangle = i(|-\rangle - |+\rangle)/\sqrt{2}$, where $|+\rangle$ and $|-\rangle$ represent the left- and right-circularly polarized components, respectively. The wave function in momentum space ($\mathbf{k}$) is specified by the following expression:

$$
|\Phi\rangle = \frac{w_0}{\sqrt{2\pi}}\exp\left[-\frac{w_0^2(k_{ix}^2 + k_{iy}^2)}{4}\right]. \qquad (8)
$$

From Eqs. (6), (7), and (8), for weak spin-orbit interaction, the reflected wave functions $|\Phi_r^H\rangle$ and $|\Phi_r^V\rangle$ can be obtained:

$$
|\Phi_r^H\rangle \approx \frac{r_{hh} - ir_{vh}}{\sqrt{2}}\exp(isk_{rx}\delta_x^H + k_{rx}\Delta_x^H)|+\rangle|\Phi\rangle
$$

$$
+ \frac{r_{hh} + ir_{vh}}{\sqrt{2}}\exp(isk_{rx}\delta_x^H + k_{rx}\Delta_x^H)|-\rangle|\Phi\rangle, \qquad (9)
$$

$$
|\Phi_r^V\rangle \approx \frac{r_{hv} - ir_{vv}}{\sqrt{2}}\exp(isk_{rx}\delta_x^V + k_{rx}\Delta_x^V)|+\rangle|\Phi\rangle
$$

$$
+ \frac{r_{hv} + ir_{vv}}{\sqrt{2}}\exp(isk_{rx}\delta_x^V + k_{rx}\Delta_x^V)|-\rangle|\Phi\rangle. \qquad (10)
$$

Here, the term of photonic spin Hall shifts can be written as

$$
\delta_x^H = \frac{r_{hh}}{k_i(r_{hh}^2 + r_{vh}^2)}\frac{\partial r_{vh}}{\partial\theta_i} - \frac{r_{vh}}{k_i(r_{hh}^2 + r_{vh}^2)}\frac{\partial r_{hh}}{\partial\theta_i}, \qquad (11)
$$

$$
\delta_x^V = \frac{r_{hv}}{k_i(r_{vv}^2 + r_{hv}^2)}\frac{\partial r_{vv}}{\partial\theta_i} - \frac{r_{vv}}{k_i(r_{vv}^2 + r_{hv}^2)}\frac{\partial r_{hv}}{\partial\theta_i}. \qquad (12)
$$

The term $\exp(isk_{rx}\delta_{rx}^{H,V})$ is the origin of the spin-orbit interaction. In general, the phases $\varphi_G = sk_{rx}\delta_{rx}^{H,V}$ can be regarded as the spin-redirection Berry phases [45–47]. It should be noted that the above approximations do not hold for strong spin-orbit interaction $\delta_{rx}^{H,V} \approx w_0$.

The spatial and angular optical signatures of the wave packet at the initial position ($z_r = 0$) are given by

$$
\langle\Delta x_\pm^{H,V}\rangle = \frac{\langle\Phi_{r\pm}^{H,V}|i\partial_{k_{rx}}|\Phi_{r\pm}^{H,V}\rangle}{\langle\Phi_{r\pm}^{H,V}|\Phi_{r\pm}^{H,V}\rangle}, \qquad (13)
$$
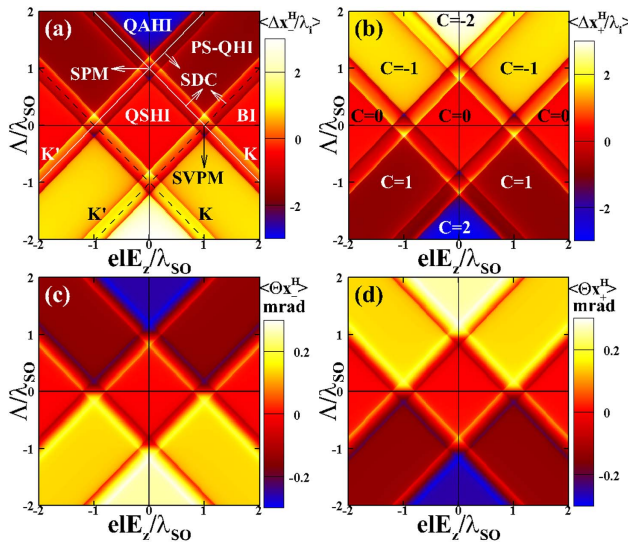
Fig. 3. Phase diagrams of (a) right- and (b) left-circular photonic Hall spatial shifts are given in the $(elE_z, \Lambda)/\lambda_{SO}$ plane, and the Chern number $\mathcal{C}$ is indicated. The (c) right- and (d) left-circular photonic Hall angular deviations are described in the topological phase diagram. The lines outline the phase boundaries indexed by K_η. The solid line represents the $s = \uparrow$, and the dashed line represents the $s = \downarrow$. The wavelength is 810 nm.

$$\langle \Theta x_\pm^{H,V} \rangle = \frac{1}{k_i} \frac{\langle \Phi_{r\pm}^{H,V} | k_{rx} | \Phi_{r\pm}^{H,V} \rangle}{\langle \Phi_{r\pm}^{H,V} | \Phi_{r\pm}^{H,V} \rangle}. \tag{14}$$

Substituting Eqs. (9) and (10) into Eqs. (13) and (14), the in-plane photonic spin Hall shifts can be written as

$$\langle \Delta x_s^{H,V} \rangle = -s \operatorname{Re}[\delta_x^{H,V}], \tag{15}$$

$$\langle \Theta x_s^{H,V} \rangle = -\frac{1}{z_R} s \operatorname{Im}[\delta_x^{H,V}]. \tag{16}$$

Here, $z_R = \pi w_0^2 / \lambda$ is the Rayleigh range, and w_0 is the beam waist. The optical signature also manifests itself as an in-plane photonic SHE whose magnitude of spatial shifts (angular deviations) reaches the order of incident wavelength (one tenth of mrad). The effect of topological phase transition in photonic SHE is clearly influenced for infrared frequencies (in the range shown $0.44 < \operatorname{Re}[\epsilon] < 1.52$ and $\operatorname{Im}[\epsilon] < 0.09$). Figure 3 shows that the topological phase diagram can be clearly described by optical signatures, whether it is spatial splitting [Figs. 3(a) and 3(b)] or angular deviations [Figs. 3(c) and 3(d)] of the reflected beam. Due to the spin-dependent nature of photonic SHE, a different Chern number can also be described.

3. SPATIAL AND ANGULAR SHIFT SIGNAL ESTIMATION

Actually, this tiny original signature needs to be amplified. Considering its practicality, using weak measurement to amplify the signature is essential [48–50]. After the preselected state, weak interaction, and post-selected state, the wave function evolves to the final state:

$$
\begin{aligned}
|\Phi_f\rangle &= \langle \psi_f | \exp(i\sigma_z k_{rx} \delta_{rx}) | \psi_i \rangle |\Phi\rangle \\
&= \langle \psi_f | 1 + i\sigma_z k_{rx} \delta_{rx} | \psi_i \rangle |\Phi\rangle \\
&\approx \langle \psi_f | \psi_i \rangle \left(1 + i k_{rx} \delta_{rx} \frac{\langle \psi_f | \sigma_z | \psi_i \rangle}{\langle \psi_f | \psi_i \rangle} \right) |\Phi\rangle \\
&= \langle \psi_f | \psi_i \rangle (1 + i k_{rx} A_w \delta_{rx}) |\Phi\rangle.
\end{aligned}
\tag{17}
$$

Here, A_w is the weak value and can be written as

$$A_w = \frac{\langle \psi_f | \sigma_z | \psi_i \rangle}{\langle \psi_f | \psi_i \rangle}, \tag{18}$$

where ψ_i is the initial state, called the preselection, and ψ_f is the final state, called the postselection:

$$\operatorname{Im}[A_w \delta_{rx}^{H,V}] = \operatorname{Re}[A_w] \operatorname{Im}[\delta_{rx}^{H,V}] + \operatorname{Im}[A_w] \operatorname{Re}[\delta_{rx}^{H,V}], \tag{19}$$

$$\operatorname{Re}[A_w \delta_{rx}^{H,V}] = \operatorname{Re}[A_w] \operatorname{Re}[\delta_{rx}^{H,V}] - \operatorname{Im}[A_w] \operatorname{Im}[\delta_{rx}^{H,V}]. \tag{20}$$

Here, the amplified angular and spatial shifts are determined by the imaginary and real parts of the weak values.

To obtain a clear picture, we represent the preselection and postselection of the states on a Bloch sphere as shown in Fig. 4. The preselected state can be written as

$$|\psi_i\rangle = \cos\left(\frac{\Theta}{2}\right)|+\rangle + e^{-i\Phi} \sin\left(\frac{\Theta}{2}\right)|-\rangle, \tag{21}$$

where $0 \leq \Theta \leq \pi$ and $0 \leq \Phi \leq 2\pi$ represent the quantum state on the Bloch sphere [51]. Due to the polarized rotation effect, we introduce a middle polarization state:

$$|\psi_m\rangle = \cos\left(\frac{\Theta}{2} + \alpha\right)|+\rangle + e^{-i(\Phi+2\delta)} \sin\left(\frac{\Theta}{2} + \alpha\right)|-\rangle. \tag{22}$$

Here, $\alpha = \arctan(|r_{hv}|/|r_{hh}|)$ and $\delta = [\arg(r_{hv}) - \arg(r_{hh})]/2$ are the polarized rotation angles for $|H\rangle$ polarization. After the postselection, the final polarization state can be written as
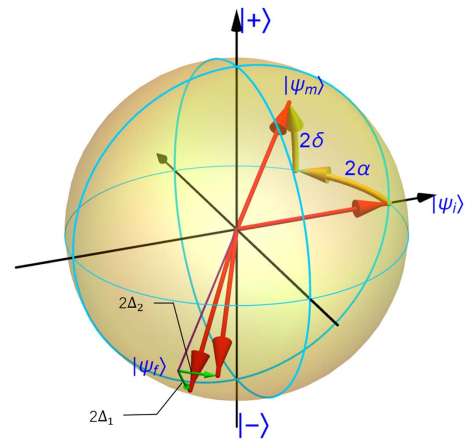
Fig. 4. Representation on the Bloch sphere of the preselection $|\psi_i\rangle$ and postselection $|\psi_f\rangle$ states. A middle state $|\psi_m\rangle$ is considered due to the polarized rotation effect. The angle $\Delta_1(\Delta_2)$ gives the origin to the real (imaginary) parts of the weak value.

$$|\psi_f\rangle = \sin\left(\frac{\Theta}{2} + \alpha + \Delta_1\right)|+\rangle$$

$$- e^{-i(\Phi+2\delta+2\Delta_2)}\cos\left(\frac{\Theta}{2} + \alpha + \Delta_1\right)|-\rangle, \quad \textbf{(23)}$$

where Δ_1 and Δ_2 are the postselection angles. A condition for weak measurements is that the two polarization states $|\psi_i\rangle$ and $|\psi_f\rangle$ are required to be perpendicular to each other [52]. Therefore, a middle polarization state is introduced, and the weak value A_w should be modified as

$$A_w = \frac{\langle\psi_f|\sigma_z|\psi_m\rangle}{\langle\psi_f|\psi_m\rangle}. \quad \textbf{(24)}$$

The probability of the postselection on $\langle\psi_f|$ and the weak value take the form

$$\gamma \approx |\langle\psi_f|\psi_m\rangle|^2 = \cos^2\Delta_2\,\sin^2\Delta_1$$
$$+ \sin^2\Delta_2\,\sin^2(\Theta + \Delta_1 + 2\alpha), \quad \textbf{(25)}$$

$$\mathrm{Re}[A_w] = \frac{\sin\Delta_1\,\sin(2\alpha + \Delta_1 + \Theta)}{|\langle\psi_f|\psi_m\rangle|^2}, \quad \textbf{(26)}$$

$$\mathrm{Im}[A_w] = \frac{\sin 2\Delta_2\,\sin(2\alpha + \Theta)\,\sin[2(\alpha + \Delta_1) + \Theta]}{2|\langle\psi_f|\psi_m\rangle|^2}. \quad \textbf{(27)}$$

After a free evolution, the wave packet evolves to its final position:

$$\langle\Delta x_w^{H,V}\rangle = \frac{\langle\Phi_f|i\partial_{k_{rx}}|\Phi_f\rangle}{\langle\Phi_f|\Phi_f\rangle}, \quad \textbf{(28)}$$

$$\langle\Theta x_w^{H,V}\rangle = \frac{1}{k_i}\frac{\langle\Phi_f|k_{rx}|\Phi_f\rangle}{\langle\Phi_f|\Phi_f\rangle}. \quad \textbf{(29)}$$

Note that the angle Δ_1 (Δ_2) is responsible for the real (imaginary) part of the weak value. If only purely real weak value is considered, we could make $\Delta_2 = 0$. Then, $\gamma = \sin^2\Delta_1$ and $A_w = \sin(2\alpha + \Delta_1 + \Theta)/\sin\Delta_1$. From Eqs. (28) and (29), the amplified shifts for $|H\rangle$ and $|V\rangle$ polarization are given by

$$\langle\Delta x_w^{H,V}\rangle = \mathrm{Re}[A_w\delta_{rx}^{H,V}] = \mathrm{Re}[\delta_{rx}^{H,V}]\frac{\sin(2\alpha + \Delta_1 + \Theta)}{\sin\Delta_1},$$
$$\textbf{(30)}$$

$$\langle\Theta x_w^{H,V}\rangle = \frac{1}{z_R}\mathrm{Im}[A_w\delta_{rx}^{H,V}] = \mathrm{Im}[\delta_{rx}^{H,V}]\frac{\sin(2\alpha + \Delta_1 + \Theta)}{z_R\sin\Delta_1}.$$
$$\textbf{(31)}$$

Moreover, if only a purely imaginary weak value is considered, we could make $\Delta_1 = 0$. So, $\gamma = \sin^2\Delta_2\,\sin^2(\Theta + 2\alpha)$ and $A_w = -i\cot\Delta_2$. Similarly, the amplified spatial and angular shifts can be obtained.

Here, the weak value can bring the spatial shifts (angular shifts) to the order of millimeters (milliradians). Based on the angular spectrum theory, the optimum of weak measurement can be obtained [53]. In Figs. 5(a) and 5(b), the optimum points (Δ_1, Δ_2) of amplified spatial shifts are close to points

(a)

(b)
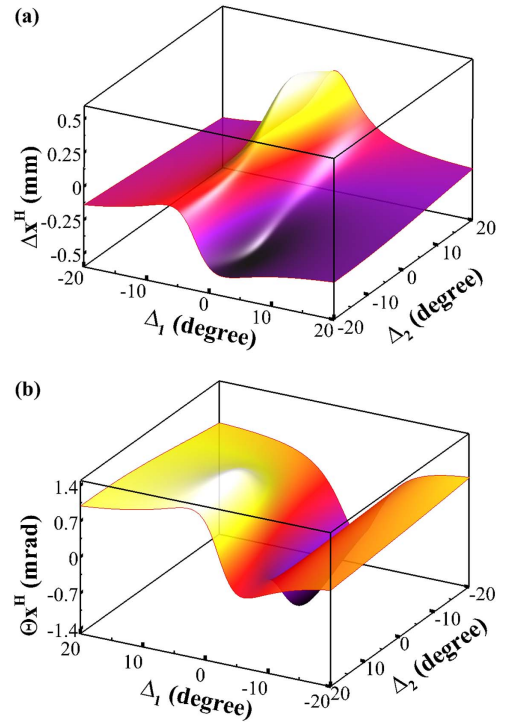
Fig. 5. The optical signature is amplified by the quantum weak measurement technique. The (a) spatial and (b) angular photonic spin Hall shifts as a function of the postselected angles. Furthermore, the Δ_1 and Δ_2 correspond to the small changes in longitude and latitude on the Bloch sphere, respectively.

(–2, 10) and (2, – 10). Further, the optimum of amplified angular shifts is close to point (2, 10) and (–2, – 10), respectively. Near the optimum point, the detected spatial (angular) shifts are about 50 (10) times larger than the initial values.

The spatial intensity profiles in different states are shown in Fig. 6. Figures 6(a)–6(f) show the gain effects of weak measurement and the result of interfering destructively in weak measurement. There is a trade-off in using the weak value to amplify the tiny signal: the sacrifice lies in a loss of energy. Note that the shifts refer to the distance from the centroid of reflected field to the center of the reflection coordinate system. Figure 6(a) shows the original intensity distribution I for $|H\rangle$ polarization in the state of QSHI. Due to the spin-orbit interaction, the unperturbed photons exhibit tiny spin-dependent splits. Subsequently, the postselection technique is used to act on the spin state of the photons, as shown in Fig. 6(d). We normalize the unperturbed intensity so that the loss of energy can be more intuitively reflected. From Figs. 6(g)–6(i), since the topological states are protected, the optical signal is stable at the low-energy region. When Λ is increased, the gap is closed; the system also becomes an intermediate state in Figs. 6(b) and 6(e), namely, the state of SPM. Simultaneously, the steady state of the signature is also broken, that is, the shifts change. Finally, Λ is further increased, the bandgap is reopened, and the topological phase transition occurs; then, the Chern number changes, as shown in Figs. 6(c) and 6(f). This means that the signature is protected by the new topological state, that is, the state of QAHI. The shift
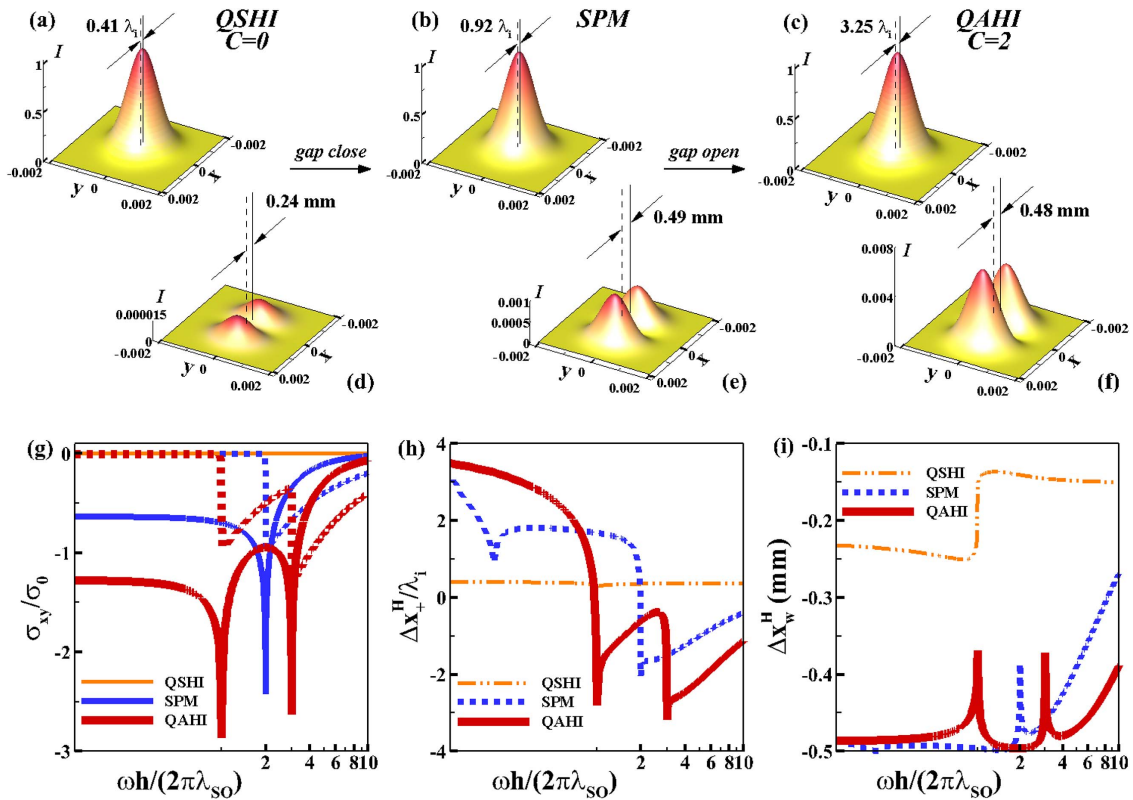
Fig. 6. Comparisons between an unperturbed and postselected intensity I distribution in different states. The intensity distribution and shifts of field centroid in the state of (a) QSHI, (b) SPM, and (c) QAHI. (d)–(f) Signal amplified by weak measurement technique. The real (solid) and imaginary (dashed) parts of the Hall conductivity are depicted in (g). (h) The original signal and (i) the amplified signal as a function of photon energy. The parameters are $\Lambda/\lambda_{SO} = 0$ (QSHI), 1 (SPM), and 2 (QAHI). $elE_z/\lambda_{SO} = 0$.

is restabilized. Comparing Figs. 6(h) with 6(i), the signature differences in different topological states are further amplified due to the weak measurement technique. This also makes it possible to observe the topological phase transition via convenient and direct optical experiment.

4. PHASE SIGNAL ESTIMATION

The weak measurement technique gives access to increase the detector's resolution. Unlike our previous scheme of using the distribution of the light field as a probe, we use the distribution of frequency to implement the phase signal estimation. The time of arrival of the photon is considered as the probe. This scheme can be used to measure the time delay in materials, depending on the polarizations. The preselection and postselection result in an amplification of the delay. The weak value serves as an amplification factor. The frequency-domain detection in weak measurement could, in principle, outperform previous standard interferometry by three orders of magnitude [25]. Here, we use this progressive method to measure 2D atomic crystals.

We have a Gaussian function $f(\omega) = (\pi\sigma^2)^{-1/4} \times \exp[-(\omega - \omega_0)^2/2\sigma^2]$ [54,55]. Since the Soleil–Babinet compensator (SBC) is responsible for weak interaction, the preselected and postselected states are different from the previous one. The preselected state is considered an elliptical polarization $|\psi_i\rangle = (e^{-i\epsilon}|H\rangle + e^{+i\epsilon}|V\rangle)/\sqrt{2}$; the postselected state

is written as $|\psi_f\rangle = (|H\rangle - |V\rangle)/\sqrt{2}$. Thus, we have a purely imaginary weak value $A_w = i \cot \epsilon$. The quantum system is the photonic polarization. The fundamental physical process is this way: photons emitted from a source with a certain spectral width pass through a polarizer and a quarter-wave plate, that is, the preselection state. The photons with an elliptically polarization state are then reflected on a topological material, which is silicene. Next, the photons pass SBC and another polarizer with postselection probability. Therefore, we have

$$|\Phi_f\rangle = \langle\psi_f| \exp(-i\tau\omega\hat{\sigma})M_r|\psi_i\rangle \otimes |\Phi\rangle$$
$$= 0.5 f(\omega)(e^{-i\tau\omega-i\epsilon}r_{hh} - e^{+i\tau\omega-i\epsilon}r_{vh}$$
$$+ e^{-i\tau\omega+i\epsilon}r_{hv} - e^{+i\tau\omega+i\epsilon}r_{vv}). \quad \text{(32)}$$

The frequency distribution is written by $F(\omega) = |\langle\Phi_f|\Phi_f\rangle|^2$. The center of frequency distribution is

$$\frac{\int \omega F(\omega)d\omega}{\int F(\omega)d\omega} = \omega_0 + \Delta\omega, \quad T = \int F(\omega)d\omega. \quad \text{(33)}$$

In Fig. 7(a), the spectral width is assumed as 100 nm. Due to the decoherence, the postselection probabilities will eventually tend to 0.5. That is to say, excessive time delays are not allowed. Fortunately, the time delay provided by SBC is significantly smaller than the decoherence time. Since topological states are protected, the decoherence rate of postselection probabilities is the same in different states. However, due to the closed gaps, the situation will be different when $\Lambda/\lambda_{SO} = \pm 1$.
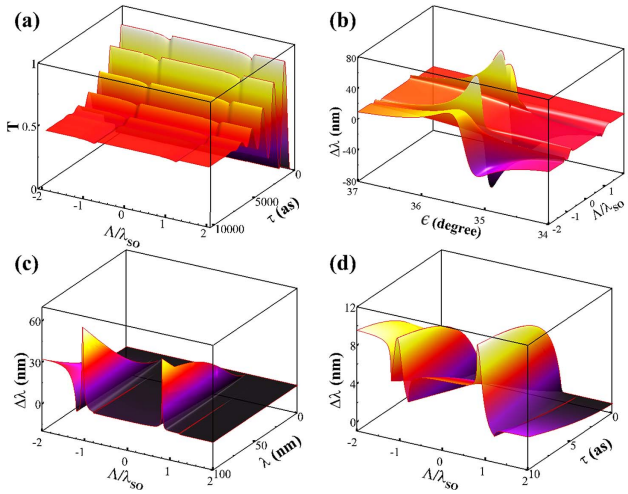
Fig. 7. (a) Postselection probability T as a function of time delay τ and the coupling constant of light Λ/λ_{SO}. Variation of the spectral shifts with (b) selected angle ϵ, (c) spectral width λ, and (d) time delay. The parameters are $E_z = 0$, and incident angle $\theta_i = 45$ deg.

The silicene is anisotropic topological materials; thus, due to the existence of cross-polarization, polarized rotation is inevitable. It can also lead to a large selected angle in preselection. In Fig. 7(b), the selected angle ϵ is close to 35.5 deg. Compared with the case without silicene, of course, there is no polarization rotation without silicene, we need to rotate the polarizer to compensate for this material-induced polarization rotation. So, as long as we can use SBC to compensate for the material-induced phase difference between $|H\rangle$ and $|V\rangle$ states, we can obtain the specific polarized rotation angle, which is caused by the material. Note that the sensitivity of weak value amplification is different in different states. When $\Lambda/\lambda_{SO} = \pm 1$, the sensitivity is the same because the bandgaps are closed.

The frequency shift $\Delta\omega$ is responsible for the spectral shift $\Delta\lambda$. We have

$$\Delta\lambda = \frac{\lambda^2}{2\pi c}\Delta\omega. \tag{34}$$

From Figs. 7(c) and 7(d), the sensitivity of spectral shifts is different in different states. However, the selected angle is different from the previous one. Because the symmetry point does not appear when $\epsilon = 0$, we can get $\epsilon = \epsilon_0 + \Delta\epsilon$. Further, $\Delta\epsilon$ is the small angle we mentioned above. The ϵ_0 is attributed to material-induced polarization rotation. By properly adjusting $\Delta\epsilon$, we can obtain the optimal weak value. In addition, the smaller spectral width or time delay will result in small phase shifts. The smaller $\Delta\epsilon$ will be more suitable.

5. CONCLUSION

In conclusion, we have discussed the optical signature in a topological phase transition. The Chern number and topological phase can be determined by the in-plane photonic spin Hall effect. Furthermore, a signature-enhancement technique known as quantum weak measurement has been theoretically proposed to enhance the original signature. Then, a phase estimation technique for 2D atomic crystals has been proposed.

Given our previous work for measuring the photonic spin Hall effect through weak measurement [56], an experimental demonstration of this work is within current capabilities. Because of the importance of measurement in topological materials, the introduction of weak measurement into topological phase transitions will significantly enrich the field of topological physics [57–59].

REFERENCES

1. M. Z. Hasan and C. L. Kane, "Colloquium: topological insulators," Rev. Mod. Phys. **82**, 3045–3067 (2010).
2. H. N. S. Krishnamoorthy, Z. Jacob, E. Narimanov, I. Kretzschmar, and V. M. Menon, "Topological transitions in metamaterials," Science **336**, 205–209 (2012).
3. W. Gao, M. Lawrence, B. Yang, F. Liu, F. Fang, B. Béri, J. Li, and S. Zhang, "Topological photonic phase in chiral hyperbolic metamaterials," Phys. Rev. Lett. **114**, 037402 (2015).
4. B. Yang, Q. Guo, B. Tremain, R. Liu, L. E. Barr, Q. Yan, W. Gao, H. Liu, Y. Xiang, J. Chen, C. Fang, A. Hibbins, L. Lu, and S. Zhang, "Ideal Weyl points and helicoid surface states in artificial photonic crystal structures," Science **359**, 1013–1016 (2018).
5. W. Zhang, X. Chen, Y. V. Kartashov, V. V. Konotop, and F. Ye, "Coupling of edge states and topological Bragg solitons," Phys. Rev. Lett. **123**, 254103 (2019).
6. T. Ozawa, H. M. Price, A. Amo, N. Goldman, M. Hafezi, L. Lu, M. C. Rechtsman, D. Schuster, J. Simon, O. Zilberberg, and I. Carusotto, "Topological photonics," Rev. Mod. Phys. **91**, 015006 (2019).
7. L. Chen, C. C. Liu, B. Feng, X. He, P. Cheng, Z. Ding, S. Meng, Y. G. Yao, and K. H. Wu, "Evidence for Dirac fermions in a honeycomb lattice based on silicon," Phys. Rev. Lett. **109**, 056804 (2012).
8. M. Ezawa, "Spin-valley optical selection rule and strong circular dichroism in silicene," Phys. Rev. B **86**, 161407 (2012).
9. C. L. Kane and E. J. Mele, "Quantum spin Hall effect in graphene," Phys. Rev. Lett. **95**, 226801 (2005).
10. C. L. Kane and E. J. Mele, "Z_2 topological order and the quantum spin Hall effect," Phys. Rev. Lett. **95**, 146802 (2005).
11. N. D. Drummond, V. Zólyomi, and V. I. Fal'ko, "Electrically tunable band gap in silicene," Phys. Rev. B **85**, 075423 (2012).
12. M. Ezawa, "Valley-polarized metals and quantum anomalous Hall effect in silicene," Phys. Rev. Lett. **109**, 055502 (2012).
13. S. A. Skirlo, L. Lu, Y. Igarashi, Q. Yan, J. Joannopoulos, and M. Solja, "Experimental observation of large Chern numbers in photonic crystals," Phys. Rev. Lett. **115**, 253901 (2015).
14. Y. Aharonov, D. Z. Albert, and L. Vaidman, "How the result of a measurement of a component of the spin of a spin-1/2 particle can turn out to be 100," Phys. Rev. Lett. **60**, 1351–1354 (1988).
15. X. Ling, X. Zhou, K. Huang, Y. Liu, C. W. Qiu, H. Luo, and S. Wen, "Recent advances in the spin Hall effect of light," Rep. Prog. Phys. **80**, 066401 (2017).
16. O. Hosten and P. Kwiat, "Observation of the spin Hall effect of light via weak measurements," Science **319**, 787–790 (2008).
17. G. Jayaswal, G. Mistura, and M. Merano, "Observation of the Imbert-Fedorov effect via weak value amplification," Opt. Lett. **39**, 2266–2269 (2014).
18. G. Jayaswal, G. Mistura, and M. Merano, "Observing angular deviations in light-beam reflection via weak measurements," Opt. Lett. **39**, 6257–6260 (2014).
19. W. J. M. Kort-Kamp, F. J. Culchac, R. B. Capaz, and F. A. Pinheiro, "Photonic spin Hall effect in bilayer graphene moiré superlattices," Phys. Rev. B **98**, 195431 (2018).

20. S. Chen, X. Ling, W. Shu, H. Luo, and S. Wen, "Precision measurement of the optical conductivity of atomically thin crystals via the photonic spin Hall effect," Phys. Rev. Appl. **13**, 014057 (2020).

21. M. C. Chang and M. F. Yang, "Optical signature of topological insulators," Phys. Rev. B **80**, 113304 (2009).

22. O. G. Rodríguez-Herrera, D. Lara, K. Y. Bliokh, E. A. Ostrovskaya, and C. Dainty, "Optical nanoprobing via spin-orbit interaction of light," Phys. Rev. Lett. **104**, 253601 (2010).

23. S. Chen, C. Mi, W. Wu, W. Zhang, W. Shu, H. Luo, and S. Wen, "Weak-value amplification for Weyl-point separation in momentum space," New J. Phys. **20**, 103050 (2018).

24. W. J. M. Kort-Kamp, "Topological phase transitions in the photonic spin Hall effect," Phys. Rev. Lett. **119**, 147401 (2017).

25. N. Brunner and C. Simon, "Measuring small longitudinal phase shifts: weak measurements or standard interferometry?" Phys. Rev. Lett. **105**, 010405 (2010).

26. X. Yin, Z. Ye, J. Rho, Y. Wang, and X. Zhang, "Photonic spin Hall effect at metasurfaces," Science **339**, 1405–1407 (2013).

27. W. Zhang, W. Wu, S. Chen, J. Zhang, X. Ling, W. Shu, H. Luo, and S. Wen, "Photonic spin Hall effect on the surface of anisotropic two-dimensional atomic crystals," Photon. Res. **6**, 511–516 (2018).

28. K. Y. Bliokh and Y. P. Bliokh, "Conservation of angular momentum, transverse shift, and spin Hall effect in reflection and refraction of an electromagnetic wave packet," Phys. Rev. Lett. **96**, 073903 (2006).

29. K. Y. Bliokh, D. Smirnova, and F. Nori, "Quantum spin Hall effect of light," Science **348**, 1448–1451 (2015).

30. H. Luo, S. Wen, W. Shu, Z. Tang, Y. Zou, and D. Fan, "Spin Hall effect of a light beam in left-handed materials," Phys. Rev. A **80**, 043810 (2009).

31. L. Cai, M. Liu, S. Chen, Y. Liu, W. Shu, H. Luo, and S. Wen, "Quantized photonic spin Hall effect in graphene," Phys. Rev. A **95**, 013809 (2017).

32. W. J. M. Kort-Kamp, B. Amorim, G. Bastos, F. A. Pinheiro, F. S. S. Rosa, N. M. R. Peres, and C. Farina, "Active magneto-optical control of spontaneous emission in graphene," Phys. Rev. B **92**, 205415 (2015).

33. W. J. M. Kort-Kamp, N. A. Sinitsyn, and D. A. R. Dalvit, "Quantized beam shifts in graphene," Phys. Rev. B **93**, 081410 (2016).

34. W. Wu, W. Zhang, S. Chen, X. Ling, W. Shu, H. Luo, S. Wen, and X. Yin, "Transitional Goos-Hänchen effect due to the topological phase transitions," Opt. Express **26**, 23705–23713 (2018).

35. D. N. Sheng, Z. Y. Weng, L. Sheng, and F. D. M. Haldane, "Quantum spin-Hall effect and topologically invariant Chern numbers," Phys. Rev. Lett. **97**, 036808 (2006).

36. E. Prodan, "Robustness of the spin-Chern number," Phys. Rev. B **80**, 125327 (2009).

37. M. Ezawa, "Photoinduced topological phase transition and a single dirac-cone state in silicene," Phys. Rev. Lett. **110**, 026603 (2013).

38. Q. D. Jiang, H. Jiang, H. Liu, Q. F. Sun, and X. C. Xie, "Topological Imbert-Fedorov shift in Weyl semimetals," Phys. Rev. Lett. **115**, 156602 (2015).

39. S. A. Yang, H. Pan, and F. Zhang, "Chirality-dependent Hall effect in Weyl semimetals," Phys. Rev. Lett. **115**, 156603 (2015).

40. R. Kubo, "Statistical-mechanical theory of irreversible processes. I. General theory and simple applications to magnetic and conduction problems," J. Phys. Soc. Jpn. **12**, 570–586 (1957).

41. L. Stille, C. J. Tabert, and E. J. Nicol, "Optical signatures of the tunable band gap and valley-spin coupling in silicene," Phys. Rev. B **86**, 195405 (2012).

42. P. Rodriguez-Lopez, W. J. M. Kort-Kamp, D. Dalvit, and L. M. Woods, "Casimir force phase transitions in the graphene family," Nat. Commun. **8**, 14699 (2017).

43. M. Liu, L. Cai, S. Chen, Y. Liu, H. Luo, and S. Wen, "Strong spin-orbit interaction of light on the surface of atomically thin crystals," Phys. Rev. A **95**, 063827 (2017).

44. W. Wu, S. Chen, C. Mi, W. Zhang, H. Luo, and S. Wen, "Giant quantized Goos-Hänchen effect on the surface of graphene in the quantum Hall regime," Phys. Rev. A **96**, 043814 (2017).

45. M. V. Berry, "Quantal phase factors accompanying adiabatic changes," Proc. R. Soc. London Ser. A **392**, 45–57 (1984).

46. K. Y. Bliokh, F. J. Rodríguez-Fortuño, F. Nori, and A. V. Zayats, "Spin-orbit interactions of light," Nat. Photonics **9**, 796–808 (2015).

47. L. Shiand and J. C. W. Song, "Shift vector as the geometric origin of beam shifts," Phys. Rev. B **100**, 201405 (2019).

48. I. M. Duck, P. M. Stevenson, and E. C. G. Sudarshan, "The sense in which a 'weak measurement' of a spin -1/2 particle's spin component yields a value 100," Phys. Rev. D **40**, 2112–2117 (1989).

49. N. W. M. Ritchie, J. G. Story, and R. G. Hulet, "Realization of a measurement of a 'weak value'," Phys. Rev. Lett. **66**, 1107–1110 (1991).

50. J. Dressel, M. Malik, F. M. Miatto, A. N. Jordan, and R. W. Boyd, "Colloquium: understanding quantum weak values: basics and applications," Rev. Mod. Phys. **86**, 307–316 (2014).

51. A. N. Jordan, J. Martnez-Rincón, and J. C. Howell, "Technical advantages for weak-value amplification: when less is more," Phys. Rev. X **4**, 011031 (2014).

52. H. Luo, X. Zhou, W. Shu, S. Wen, and D. Fan, "Enhanced and switchable spin Hall effect of light near the Brewster angle on reflection," Phys. Rev. A **84**, 043806 (2011).

53. X. Zhou, X. Li, H. Luo, and S. Wen, "Optimal preselection and postselection in weak measurements for observing photonic spin Hall effect," Appl. Phys. Lett. **104**, 051130 (2014).

54. C.-F. Li, X.-Y. Xu, J.-S. Tang, J.-S. Xu, and G.-C. Guo, "Ultrasensitive phase estimation with white light," Phys. Rev. A **83**, 044102 (2011).

55. X.-Y. Xu, Y. Kedem, K. Sun, L. Vaidman, C.-F. Li, and G.-C. Guo, "Phase estimation with weak measurement using a white light source," Phys. Rev. Lett. **111**, 033604 (2013).

56. S. Chen, X. Zhou, C. Mi, H. Luo, and S. Wen, "Modified weak measurements for the detection of the photonic spin Hall effect," Phys. Rev. A **91**, 062105 (2015).

57. P. N. Dyachenko, S. Molesky, A. Yu Petrov, M. Störmer, T. Krekeler, S. Lang, M. Ritter, Z. Jacob, and M. Eich, "Controlling thermal emission with refractory epsilon-near-zero metamaterials via topological transitions," Nat. Commun. **7**, 11809 (2016).

58. C. Shang, X. Chen, W. Luo, and F. Ye, "Quantum anomalous Hall-quantum spin Hall effect in optical superlattices," Opt. Lett. **43**, 275–278 (2018).

59. H. Wang, B. Yang, W. Xu, Y. Fan, Q. Guo, Z. Zhu, and C. T. Chan, "Highly degenerate photonic flat bands arising from complete graph configurations," Phys. Rev. A **100**, 043841 (2019).